J. Appl. Comput. Mech., 4(4) (2018) 318-330
DOI: 10.22055/JACM.2018.24339.1183

ISSN: 2383-4536
jacm.scu.ac.ir

Shahid Chamran University of Ahvaz

Journal of Applied and Computational Mechanics

Research Article

A Study of Model Separation Flow Behavior at High Angles of Attack Aerodynamics

A. Roy, A. K. Mallik, T. P. Sarma

Department of Applied Mechanics, Indian Institute of Technology, Madras, Chennai 600036, India

Received December 08 2017; Revised February 14 2018; Accepted for publication March 17 2018.
Corresponding author: Aritras Roy, aritrasroy73@gmail.com

Abstract. This paper analyzes the aerodynamic performance and flow separation characteristics of a rectangular wing for varying Reynolds numbers. The mechanism of separation and its effect on the rectangular wing were simulated in ANSYS FLUENT using K-ω SST turbulence model. A detailed analysis was performed to discuss aspects like the lift and drag force of the wing surface, surface pressure distribution around the wing surface, flow separation characteristics for different angles of attack, velocity profiles at different sections of the wing surface along the chord length, and the effect of wing tip vortices. The simulation results showed that by increasing the angles of attack, the separation point moves towards the leading edge and the onset of stalling is very much closer to the leading edge. Also, the experimental and numerical results indicated that NACA4415 airfoil had enhanced coefficient of lift to coefficient of drag ratio at the angles of attack (AoA) ranging between 4° and6°, which are distinctively advantageous for the better performance of small-scale wind turbine rotors. The experimental and computational results were analyzed in the context of effective change in stalling characteristics at different Reynolds numbers.

Keywords: Flow separation, Tip vortices, Gentle stall, Laminar separation bubble, Backflow.

1. Introduction

Recent interests in designing Micro Aerial Vehicles (MAVs) and wind turbine blades at low Re for small Horizontal Axis Wind Turbine (HAWT) applications have revived research on the performance of airfoils like NACA4415 at relatively low Reynolds numbers. A common problem with a low Reynolds number flow over airfoil is that separation is almost inevitable. This research is focused on studying the separated flow regime, the unsteady model separated flow and the several parameters contributing to its separation including the angles of attack, the turbulence of the free stream, and the shape and motion of the wing. Prediction of separated flow over wings at high angles of attack is itself resource intensive.

For relatively low Re flows, the laminar separation bubble (LSB) due to adverse pressure gradients is found to be the cause of flow separation behavior, which appears at relatively higher angles of attack. Depending on its size and behavior, it deteriorates the aerodynamic performance of the wing [1], [2]. It also plays an important role in defining the behavior of the boundary layer separation and the stalling characteristics of the airfoil [1]. Sharma and Poddar [3] investigated on NACA0015 airfoil and reported the occurrence of abrupt stall due to the bursting of the bubble after reaching certain AoA.

Typical airfoils which are designed basically for high Reynolds numbers, such as the NACA airfoil 4-digit series, are reported to underperform for such low Reynolds number conditions and, consequently, degrade the wind turbine performance [4], [5]. Turbulence modeling of this kind of aerodynamic flow is also a challenging task. Different turbulence models are used for prediction but each has its limitations. Several researchers have tried to find the most suitable model which can predict the separated regime for flow over a 3D wing. It has been found that computational fluid dynamics (CFD) models based on

Published Online: October 11 2018

Reynolds-averaged Navier–Stokes (RANS) can predict with lower risks of inaccuracy [6-10]. The two-equation K-ω model has some distinctive advantages which can be further improved with the BLS model [10]. The separated flow regime can also be found out from Von Karman boundary layer Integral equation by equating skin friction coefficient to be zero [14]. Separation of the flow is assumed to occur when H reaches a value between 1.8 and 2.4. The value of H increases rapidly near separation, and then begins to decrease. The point corresponding to the maximum value of H is taken as the separation point [24].

Laminar flow separation is usually found on low-Reynolds-number airfoils when laminar boundary layers are unable to withstand adverse pressure gradients. The post-separation behavior of laminar boundary layers affects the aerodynamic performance of low-Reynolds-number airfoils by increasing the drag and decreasing the lift. For lower AoA, the increment of the airfoil lift coefficient was found to be almost the same as predicted based on thin airfoil theory, which results in a very small drag coefficient of the airfoil [15]. The small increment of drag in drag polar plot is described as bubble drag" at AoA 4°-6° [21], which is the cause of formation of LSB. Different experimental investigations have been carried out for laminar flow separation, transition, and reattachment on low-Reynolds-number airfoils. All these estimated separation regimes are based on point-wise flow diagnostic techniques [16] [18].

The laminar boundary layer was found to attach to the airfoil suction surface from the airfoil leading edge to the trailing edge when the adverse pressure gradient over the suction surface of the airfoil is mild at relatively small AoAs [20]. The increase of efficiency at gradual stall condition is necessary for wind turbine blades and thick airfoils are best suitable as they sohw desirable performance under variable inflow conditions [26].

In this study, numerical simulations have been done to investigate the effect of wing tip vortices on an unswept and untwisted rectangular wing (NACA4415) at different geometric angle of attacks using the ANSYS FLUENT and the numerical results have been compared with the experimental measurements. Moreover, this paper puts computational effort towards understanding flow physics on NACA4415 airfoil at relatively low Re values using the RANS-based K-ω SST model. This model was chosen as it has the clear advantage of associating transition model and much attention has been paid to understanding the model separated flow and its direct consequences on the aerodynamic performance of the wing. The overall goal of this paper is to perform numerical simulations for pitching motion involved in the study and comparing the results with the model separated flow.

2. Experimental Facility

The experiment was carried out in a suction type wind tunnel. The wind tunnel was in Aerospace Engineering Department, IIT Madras. All the details of the experimental techniques and the models used are given below.

2.1 Model Description

The wing used in this experiment has NACA4415 airfoil section with chord length(c) =6.3cm and span (b) =40 cm. The material used for the model wing is carbon polymer as it is light. The aspect ratio of the wing model is 6 and the rotation of the wing model was controlled by a turning table through an opening on the tunnel floor.

2.2 Wind Tunnel Facility

The experiments were conducted at an open circuit, suction type subsonic wind tunnel. The tunnel consisted of six main parts, namely honeycomb section, setting chamber, contraction cone, test section, diffuser, and drive section. The dimensions of the test section of the wind tunnel were $0.5m \times 0.5m \times 2m$. The tunnel had transparent windows on both the top and the side walls for studying flow visualization. A six-bladed fan was installed downstream of the test section rotated by a 5 HP rotor to produce the suction. The schematic diagram of the wind tunnel is shown in Fig.1.

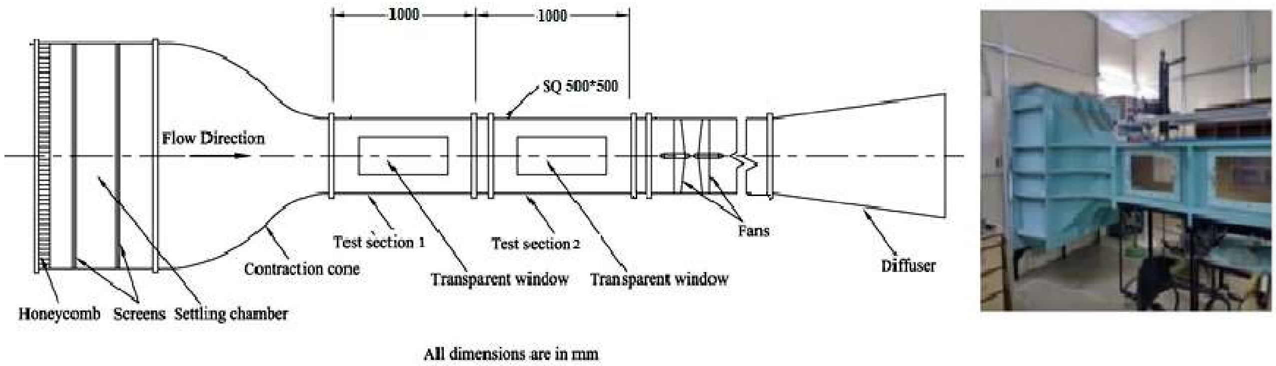

Fig. 1. Laboratory wind tunnel

2.3 Experimental Procedure

A Three-component load balance (make: Sunshine Measurements) consisting of a balance mechanism, strain gauge instrument amplifiers and a microcontroller-based measuring system were used to measure the lift and drag forces exerted on the wing model. The balancing mechanism was designed as a floor balance. The model was mounted on a stem that protrudes into the test section and was fixed on a metric plate which transfers the loads onto four Strain elements. The outputs from the Strain gauge mounted on the strain elements were then amplified. The calibration coefficients were first calculated by a relationship between the measured outputs and the physical parameters to which the instrument was subjected. The Strain gauge instrumentation was designed in the linear range of sensitivities and the calibration coefficients were then calculated from the slope of these linear variations and expressed in the following equation:

The calibration coefficients used were $D_{ij} = [1.8978\ -1.8964\ -0.21153; -19.9898\ 13.1284\ -30.9883; 0.14817\ -0.07042\ 0.85827]$.

The load balance system with the wing model was mounted on the wind tunnel after calibration and the voltages measured by the microcontroller were converted into forces (lift and drag) using the following conversion equations.

$$\text{Lift}\ (L) = \left[\left(D_{11}V_1 + D_{12}V_2 + D_{13}V_3\right)\times 1000\right]/G \tag{1}$$

$$\text{Drag}\ (D) = \left[\left(D_{21}V_1 + D_{22}V_2 + D_{23}V_3\right)\times 1000\right]/G \tag{2}$$

2.4 Uncertainty Analysis

For estimating uncertainty in experimental results, a more precise method has been presented by Kline and McClintock [39] and Moffat [38]. Suppose a set of measurements is made in which the uncertainty in each measurement is expressed with the same odds. These measurements are then used to calculate some desired result of the experiments. We wish to estimate the uncertainty in the calculated result on the basis of the uncertainties in the primary measurements. The result R is a given function of the independent variables $x_1, x_2, x_3, \ldots\ldots, x_n$. Thus,

$$R = R\left(x_1, x_2, x_3 \ldots x_n\right) \tag{3}$$

Let ω be the uncertainty in the result and $\omega_1, \omega_2, \ldots, \omega_n$ be the uncertainties in the independent variables. If the uncertainties in the independent variables are all given with the same odds, then the uncertainty in the result having these odds is given in Ref. [38, 39] as

$$\omega_R = \left[\left(\frac{\partial R}{\partial x_1}\omega_1\right)^2 + \left(\frac{\partial R}{\partial x_2}\omega_2\right)^2 + \ldots + \left(\frac{\partial R}{\partial x_n}\omega_n\right)^2\right]^{1/2} \tag{4}$$

2.5 Uncertainties for Product Function

In many cases, the result function of Eq. (4) takes the form of a product of the respective primary variables raised to exponents and expressed as

$$R = x_1^{a_1} x_2^{a_2} x_3^{a_3} \ldots\ldots\ldots x_n^{a_n} \tag{5}$$

Taking partial derivative of R with respect to x_i and inserting this in equation (5), we get

$$\frac{\omega_R}{R} = \left[\sum\left(\frac{a_i\,\omega_{x_i}}{x_i}\right)^2\right]^{1/2} \tag{6}$$

The estimated uncertainty values are calculated as stated above and shown in Table 1.

Table 1. Approximate quantities of estimated experimental quantities

Experimental quantity	Estimated Uncertainty
Velocity	1%
Lift Coefficient (C_L)	2.8%
Drag Coefficient (C_D)	3.6%

3. Numerical Methodologies

3.1 Geometry

The rectangular wing models used for simulation had a NACA4415 airfoil section with a Chord length (c) of 6.3cm, a span length (b) of 40cm and an aspect ratio of 6. The geometry of NACA 4415 was created by ANSYS design modeler. Suitable flow domain was also chosen in order to minimize the wall effect.

3.2 Meshing

Unstructured hybrid mesh grids were generated, which are combinations of tetrahedrons, wedges and pyramids using ANSYS MESHING workbench. In order to resolve properly, the boundary layer along the fluid domain walls and the15-layer inflation mesh property around the wing body were defined and the first layer thickness was adjusted for the dimensionless wall distance y^+=1. Near the wall, mesh sizes (y^+ values) were arranged appropriately to resolve the boundary velocity profile. Totally, 60975 nodes and 234880 elements were created in mesh. Mesh grid view of flow domain and mesh statistics are given in Fig. 2 and Table 2, respectively. According to mesh quality criteria of ANSYS, mesh quality improves significantly as orthogonal quality of mesh moves towards 1. For good quality of mesh, skewness of the generated mesh should also have a value close to 0.

Table 1. Mesh statistics

Mesh metric	Minimum	Maximum	Average
Orthogonal quality	1.38e-002	0.99	0.9
Skewness	1.47e-003	0.99	0.2

y^+ is the non-dimensional normal distance from the first grid point (the wall-adjacent cell center) to the wall. Near the wall, mesh sizes (y^+ values) were arranged appropriately to resolve the boundary velocity profile. Fig. 2 shows the wall y^+ value distribution over the wing surface. It shows wall y^+ value ranging from 1 to 5 for the suction surface, which signifies enhanced wall treatment is used to take care of it.

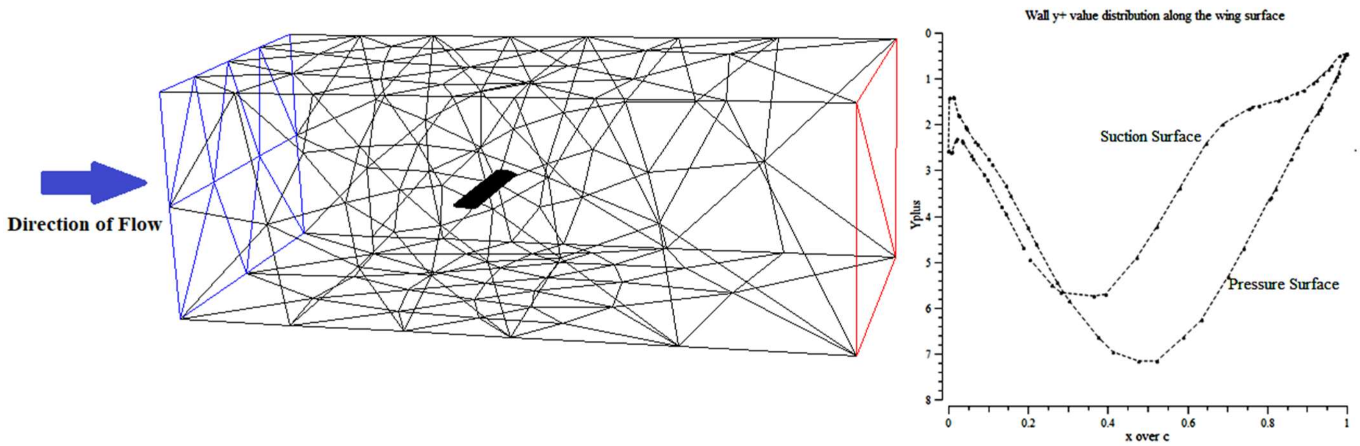

Fig. 2. Mesh grid view of flow domain and Wall y^+ value distribution along the wing surface

3.3 Governing equations

Conservation equation of mass, momentum and energy were solved to obtain solution over the rectangular wing. Conservation of mass is represented as Equation (7)

$$\frac{\partial \rho}{\partial t} + \Delta \cdot (\rho v) = 0 \tag{7}$$

From conservation of momentum we get,

$$\left.\begin{aligned} \rho\frac{Du}{Dt} &= -\frac{\partial p}{\partial x} + \frac{\partial \tau_{xx}}{\partial x} + \frac{\partial \tau_{yx}}{\partial y} + \frac{\partial \tau_{zx}}{\partial z} + \rho f_x \\ \rho\frac{Dv}{Dt} &= -\frac{\partial p}{\partial y} + \frac{\partial \tau_{xy}}{\partial x} + \frac{\partial \tau_{yy}}{\partial y} + \frac{\partial \tau_{zy}}{\partial z} + \rho f_y \\ \rho\frac{Dw}{Dt} &= -\frac{\partial p}{\partial z} + \frac{\partial \tau_{xz}}{\partial x} + \frac{\partial \tau_{yz}}{\partial y} + \frac{\partial \tau_{zz}}{\partial z} + \rho f_z \end{aligned}\right\} \tag{8}$$

3.3 Turbulence Modelling

The application of Navier-Stokes methods in aerodynamic flows is complex since these types of flows cannot be treated directly by in-viscid, or viscous in-viscid interaction schemes and thus the prediction of aerodynamic flows such as separated flows, flows with three-dimensional separation and complex unsteady flows is difficult. It is obvious that the improvement of numerical methods for aerodynamic flows must be accompanied by the development of more general turbulence models and their implementation into Navier-Stokes methods. The simplest available turbulence model is the one-equation model recently developed by Spalart and Almaras. This model basically solves one partial differential equation for eddy viscosity as turbulence viscosity. However, the method fails to produce the proper shapes of the velocity profiles. This method predicts

good results for free shear layer flows but is unfortunately too sensitive to the effect of adverse pressure gradients.
The second most popular non-algebraic turbulence models are two-equation eddy-viscosity models. These models solve two transport equations, generally one for the turbulent kinetic energy and another related to the turbulent length scale (or time scale). Among the two-equation models, the k - ε model is now the most widely-used one. It has been used widely over a long period of time but it has its own shortcomings. This model is again not sensitive to the adverse pressure gradients as it predicts the delayed separation and that is why it is not treated as an ideal model for predicting aerodynamic flows. The reason for predicting the delayed separation is the computation of ε equation near the wall region. This model shows numerical stiffness when integrated through the viscous sub layer. For low Re flows, however, K- ε model usually employs a damping function which is highly nonlinear. This non-linearity cannot be easily terminated using conventional linearization techniques and creates problem in convergence.

There has been a significant development of alternative models [31], [32] to overcome the shortcomings of the k - ε model. One of the most successful models, with respect to both accuracy and robustness, is the k - ω model of Wilcox [30]. It solves for turbulent kinetic energy (k) and turbulent dissipation rate (turbulent frequency) (ω). This model shows better sensitivity corresponds to the adverse pressure gradients. The model does not employ damping functions thus it is numerically quite stable. Its formulation of viscous sub layer is also very simple. However, this model is strongly dependent on free stream values which are outside the shear layer. The dependency of free stream values are corrected by BSL (Base line model) k – ω model which is identical to the k – ω model of Wilcox [30] for the inner region of a boundary layer and gradually changes to the high Reynolds number version.

The second version of model k – ω is called the Shear-Stress Transport (SST) model which is basically a variation of base line model with additional ability to account for the transport of the principal turbulent shear stress in adverse pressure gradient boundary layers. The inclusion of SST model corrections with k – ω model is basically to the aim of transforming it to an independent model of free stream values which show a better agreement with experimental data for adverse pressure gradient boundary-layer flows. The original k – ω model equations are as follows:

$$\frac{D\rho k}{Dt} = \tau_{ij}\frac{\partial u_i}{\partial x_j} - \beta^*\rho\omega k + \frac{\partial}{\partial x_j}\left[\left(\mu + \sigma_{k1}\mu_t\right)\frac{\partial k}{\partial x_j}\right] \tag{9}$$

$$\frac{D\rho\omega}{Dt} = \frac{\gamma_1}{v_t}\tau_{ij}\frac{\partial u_i}{\partial x_j} - \beta_1\rho\omega^2 + \frac{\partial}{\partial x_j}\left[\left(\mu + \sigma_{\omega 1}\mu_t\right)\frac{\partial \omega}{\partial x_j}\right] \tag{10}$$

with constants given by Wilcox [30]:

$$\begin{gathered}\sigma_{k2} = 1.0,\ \sigma_{\omega 2} = 0.856,\ \beta_2 = 0.0828 \\ \beta^* = 0.09,\ k = 0.41,\ \gamma_2 = \beta_2 / \beta^* - \sigma_{\omega 2}k^2/\sqrt{\beta^*}\end{gathered} \tag{11}$$

Eddy viscosity is given by:

$$v_t = \mu_t / \rho = k / \omega \tag{12}$$

Turbulent stress tensor is given by:

$$\tau_{ij} = u_i' u_j' \tag{13}$$

$$\tau_{ij} = \mu_t\left(\frac{\partial u_i}{\partial x_j} + \frac{\partial u_j}{\partial x_i} - \frac{2}{3}\frac{\partial u_k}{\partial x_k}\delta_{ij}\right) - \frac{2}{3}\rho k\,\delta_{ij} \tag{14}$$

An important effect of the SST model is the inclusion of effect of the transport of the principal turbulent shear-stress Therefore, it can be written as:

$$\frac{D\tau}{Dt} = \frac{\partial \tau}{\partial t} + \mu_k\frac{\partial \tau}{\partial x_k} \tag{15}$$

J K model [33] has introduced a transport equation for the demonstration of the SST model which uses the Bradshaw [34], [35] assumptions, where turbulent shear stress in the boundary layer is proportional to the turbulent kinetic energy.

$$\tau = \rho\alpha_1 k \tag{16}$$

Shear stress can also be computed from the two-equation model:

$$\tau = \mu_t\Omega \tag{17}$$

Therefore, Shear stress can be rewritten as:

$$\tau = \rho\sqrt{\frac{\text{Production}_k}{\text{Dissipation}_k}}\alpha_1 k \tag{18}$$

For bounded flows near the wall, however, the presence of adverse pressure gradients makes production/dissipation greater than 1, which means it is more than the predicting shear stress. As a result, eddy viscosity is redefined as:

$$v_t = \frac{\alpha_1 k}{\Omega} \tag{19}$$

This modification to the eddy-viscosity has been done in connection with the base line model (BSL). However, in order to recover the correct behavior boundary layer, the diffusion constant σ_{k1} is adjusted only with 0.85 (previously, it was 0.50) keeping all other values unchanged. Thus, it is appropriate to use k – ω SST model for an external flow like the flow over 3D wing to predict the flow behavior accurately.

3.4 Computational Technique

The numerical analysis was performed using ANSYS FLUENT software for solving the Reynolds-Averaged Navier-Stokes (RANS) equations with k – ω SST turbulence model. This model was used in conjunction with steady state solution. The two models were considered for the present study within the flow domain over NACA4415 rectangular wing. Constant properties like density and viscosity were assumed for the flow without any significant change in temperature, which is shown in Table 3. Pressure-Velocity coupling method was used to solve these models and second order upwind spatial discretization scheme was applied for momentum. Solutions were initialized uniformly throughout the domain using free stream inlet condition. Velocity inlet with a free stream velocity magnitude of 12 m/s was used as the inlet boundary condition and no-slip wall condition was applied to the model surfaces without specifying any wall roughness. To simulate the angle of attack, stream velocity directions were adjusted in accordance to the required angle of attack and the convergence criterion of 10^{-4} was selected for the residuals as ANSYS default settings.

Table 3. Parameters for numerical calculation

Gas	Air, Ideal Gas
Density	1.177 kg/m^3
Viscosity	1.846e-05 kg/m-s
Velocity	12 m/s
Temperature	300 K

4. Results and Discussions

4.1 Experimental and numerical study of lift and drag characteristics of the wing

Figures 3 and 4 show the experimental and numerical comparisons of aerodynamic performance recorded from the force measurements of a wing with the NACA4415 airfoil section at the Reynolds numbers of 0.045 and 0.1 million. The experimental results and the ANSYS FLUENT results have very similar maximum recovery of lift coefficients at approximately 16° AoA for Re= 0.045 million. For the greater Re (i.e. 0.1 million), it was found that the recovery of lift coefficient of wing was less pronounced compared to the smaller Re (0.045 million). The stalling angles, however, were more or less the same in both cases. Certain increment of lift after stalling in the post stall region was also seen for Reynolds number 0.045 million but this feature was less pronounced in the greater Reynolds number. After this initial stall", the wing tried to recover the initial stall lift coefficient, which is also quite clear from C_L versus AoA curve.

It is interesting to note that a different stalling behavior is observed by changing Reynolds numbers from 0.045 million to 0.1 million. For Re 0.045 million, leading edge stalling behavior is shown, which signifies rapid drop of lift curve near the maximum lift. For comparatively higher Reynolds number, however, trailing edge stall is found, which means the gradual bending-over of lift curve at the maximum lift. Due to the change in stalling behavior, the value of $C_{L,\,max}$ also changes. For the Re of 0.045 million, it is 1.217 (experimental), but for the Re of 0.1 million, it is 1.069 (experimental). This decrement of $C_{L,\,max}$ with an increase of Reynolds number is justified here only by the effective change in stalling characteristics.

Fig. 5 shows experimental and numerical comparisons of drag polar plot at different Reynolds no. C_L/C_D ratio increases with the increase of Reynolds numbers as expected. For Reynolds no 0.045 million, max C_L/C_D ratio is observed to be 6°, but for Reynolds no 0.1 million, it is shifted to 4° and its corresponding values of max ratio are 8.49 and 9.55, respectively (ANSYS FLUENT). On the other hand, for experimental comparison, the increase in Reynolds no does not cause any significant change in max C_L/C_D ratio (5.92). This maximum C_L/C_D value obtained at 6° and 4° are considered significant for early capture of energy for the application of wind turbine blades (Fig.5) [NACA4415 is one of the airfoils which is extensively used as a wind turbine blade]. Experimental mismatch of max C_L/C_D ratio from numerical values are justified due to higher uncertainty of drag measurement in the instrument. The reason of this increment of C_D for the smaller Reynolds number is due to the bubble drag" as identified by Selig [21]. The presence of bubble drag is associated with the laminar separation bubble (LSB) and for the smaller Reynolds number, longer bubble formation is presumably the cause of higher drag.

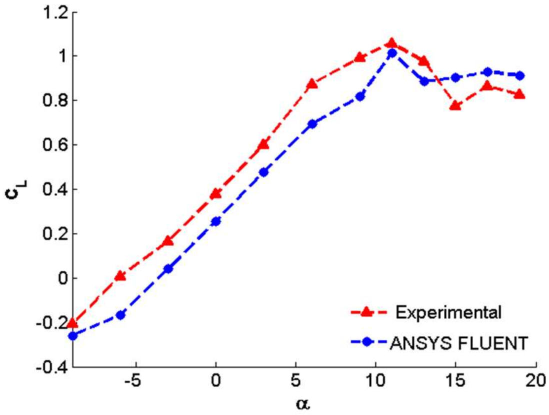

Fig. 3. C_L–AoA at Re= 0.045 million

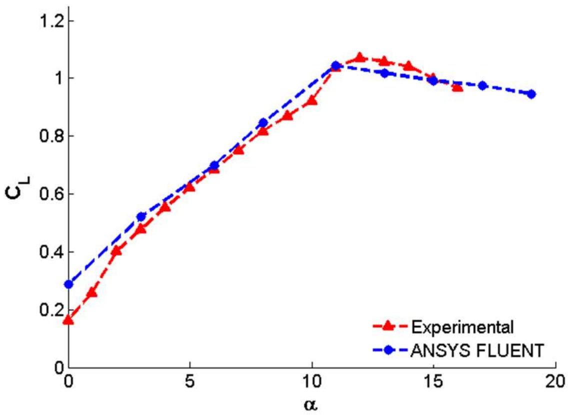

Fig. 4. C_L–AoA at Re=0.1 million

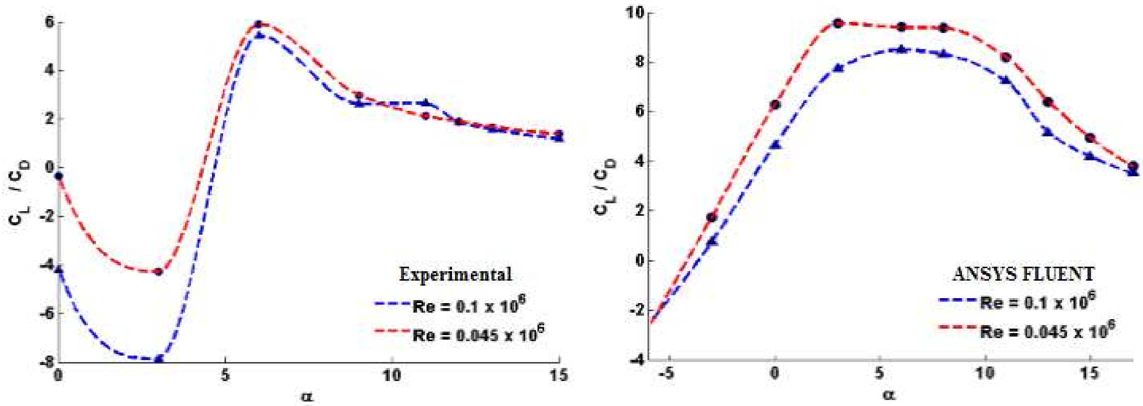

Fig. 5. Experimental and numerical comparison of drag polar plots at different Re

4.2 Pressure distribution on the wing surface

Fig.6 shows the pressure variations over the upper and lower surfaces at various incidences while the Reynolds number is kept constant (0.045 million). Basically, the discussion of pressure distributions is mainly concerned with the airflow separation over the wing. The pressure distribution on the suction surface of the airfoil is influenced by a low pressure zone at a small distance away from the leading edge and, beyond this zone pressure, it increases in the direction of airflow towards trailing edge. Due to the reduction of energy, the air fails to progress through the boundary layer against the pressure gradient, thereby separating from the surface.

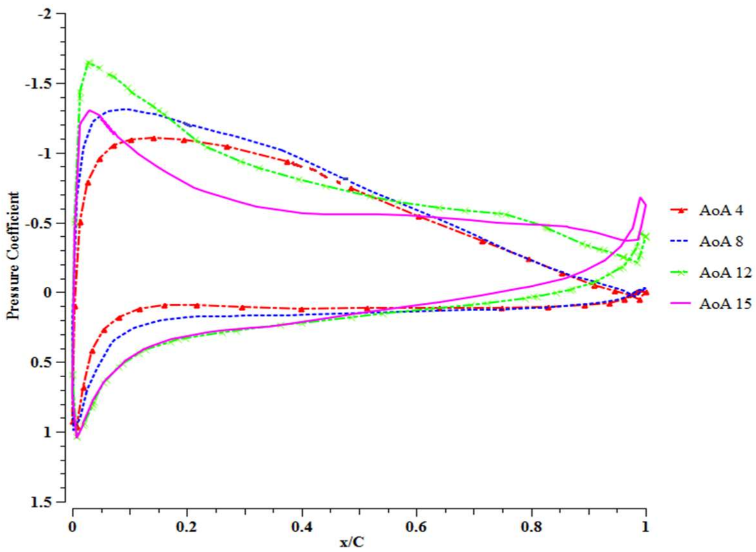

Fig. 6. Variation of pressure coefficient along the wing surface for different AoA

From Fig. 6, it can be further noted that surface pressure distribution on the pressure surface of the airfoil does not change noticeably with the increase in angles of attack up to 12° (stalling angle). The surface pressure distribution on the suction surface of the airfoil was found to vary significantly at different AoA. For the lower AoA, the surface pressure gradually recovered over the suction surface of the airfoil up to the airfoil trailing edge. As the angle of attack is extended above stall and in post-stall, a loss of suction peak is observed due to the formation of a large wake region, as predicted, by the increment of wing tip vortices diameter (Fig. 16 - Fig 19).

4.3 Point of Separation behavior on the wing suction surface

This section emphasizes on finding out the point of flow separation near the root region. To figure out the point of separation, skin friction coefficient with non-dimensional chord length has been plotted. The point where the skin friction coefficient becomes zero is marked as the point of separation (Fig.7).

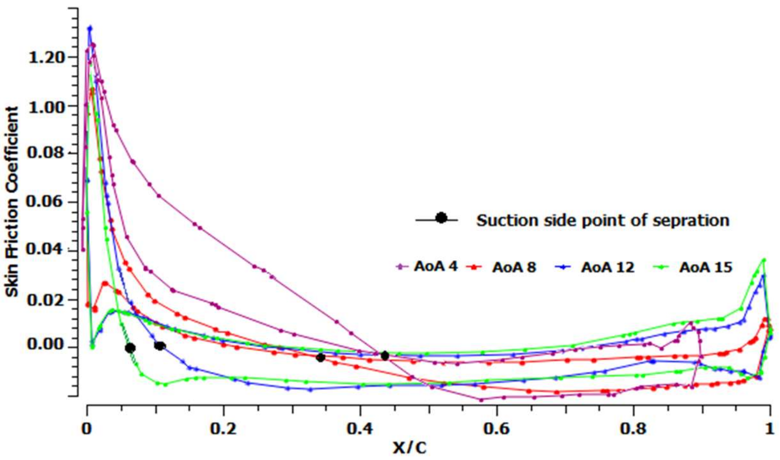

Fig. 7. Variation of skin friction coefficient along the wing surface at different AoAs

Drag force and skin friction coefficient, which is a non-dimensional measure of drag force, is greatly influenced by the flow separation. From the von Karman integral boundary-layer equation, we can write:

$$\frac{1}{\rho u_e^2\theta}\frac{d\left(\rho u_e^2\theta\right)}{d\xi}=\frac{c_f}{2\theta}-\frac{H}{u_e}\frac{du_e}{d\xi} \tag{20}$$

where ξ is the boundary-layer co-ordinate, u_e is the boundary-layer edge velocity, H is the shape factor, and θ is defined as the ratio between the boundary-layer momentum thickness and δ^* (the boundary-layer displacement thickness). Skin friction coefficient is zero at the point of separation. Then Equation (4.1) can be written as

$$\frac{\Delta\left(\rho u_e^2\theta\right)}{\rho u_e^2\theta}\simeq -H\frac{\Delta u_e}{u_e} \tag{21}$$

After simplification, Equation (4.2) is simplified as,

$$\Delta\left(\rho u_e^2\theta\right)\simeq -\rho u_e\delta^*\Delta u_e \tag{22}$$

From Equation (4.3) it can be seen that the increase in drag $\triangle\,(\rho u_e^2\theta)$ is proportional to the multiple of mass defect $(\rho u_e\delta^*)$ and the difference in edge velocity [36]. The increase of mass defect after flow separation is the cause of increment of drag and the onset of stalling is due to this rapid increment of drag. At a high AoA, the flow is separated from the wing. As the angles of attack increase, the separation point moves toward the leading edge of the wing as NACA4415 shows trailing edge stalling characteristics. This is quite obvious due to the movement of laminar separation bubble towards the leading edge. Fig.8 represents the point of separation on the wing suction surface at different angles of attack.

4.4 Discussion on Velocity Profiles

Figs. 9- 14 show the velocity profiles at different angles of attack at different sections on the airfoil. In the figures, the x axis represents the non-dimensionalized velocity ($u/u_{infinity}$) where $u_{infinity}$ is the free stream velocity. The figures show that the values of non-dimensional velocities are greater than unity. This is due to the fact that the inflation layer taken for simulation exceeds the boundary layer thickness and thus, outside the boundary layer, the simulator considers the fluid to be viscous and applies the boundary layer equations. We are taking high inflation to understand the phenomena happening at the surface of the airfoil at high angles of attack which is our main point of interest. In the figures, the starting point of the velocity profiles decreases in the y value as a result of increases in the angles of attack, which is due to the change of the location of the airfoil surface going down with the increase in the angles of attack. Again, from the figures, it can be seen that the starting points of the velocity profiles are reduced in the y values by increasing the airfoil length from the leading edge. This is due to the position of the origin of the co-ordinate frame which is located at the leading edge of the mean chord line [Fig. 9]. Thus, by increasing the length of the airfoil, the surface of the airfoil goes from positive to negative due to the orientation of the origin.

Fig.10 shows that increasing the angles of attack does not lead to any significant change in the velocity profiles because at the leading edge the flow is not separated even at higher angles of attack and on moving along the airfoil the flow separation phenomena becomes prominent.

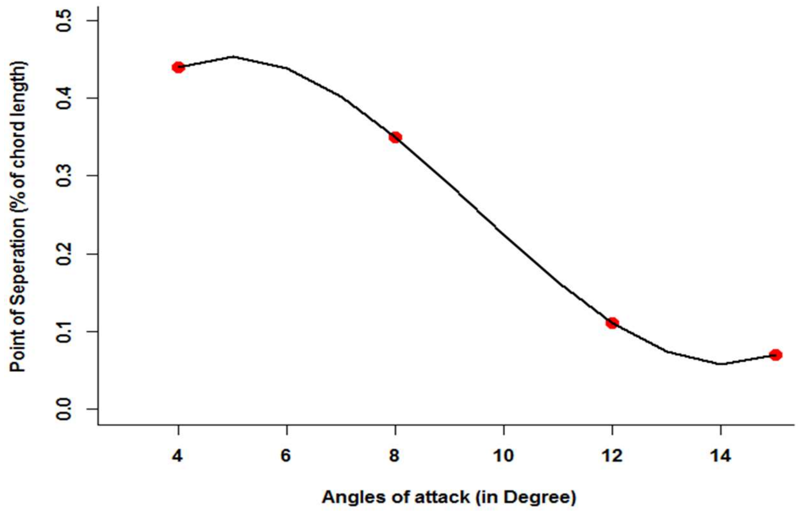

Fig. 8. Point of separations at different angles of attack

In Fig. 11, x/C = 0.3, which is little far from the leading edge, shows variation in the velocity profiles at different angles of attack whereas at the leading edge (x/C=0.15, Fig.10) there were no such significant variations in velocity profiles. The velocity profile at AoA 15° in Fig. 12 shows back flow which signifies that at 15° angle of attack, the flow is separated at that position which is at the root of the airfoil, but the velocity profile at AoA 12° does not show backflow, although it is in the verge of reversing its direction. Therefore, 12° angle of attack is taken as the stall angle for this particular airfoil NACA4415. At 15° AoA, the back flow is quite clear in the figures. Figs.1314 show a prominent view of back flow at angles 12° and 15°, which confirms the flow separation at angles of attack 12° or higher. Fig.14 represents the section very close to the trailing edge where there is a back flow at 8° also along with 12° and 15° which is due to the formation of vortices at the trailing edge of the wing.

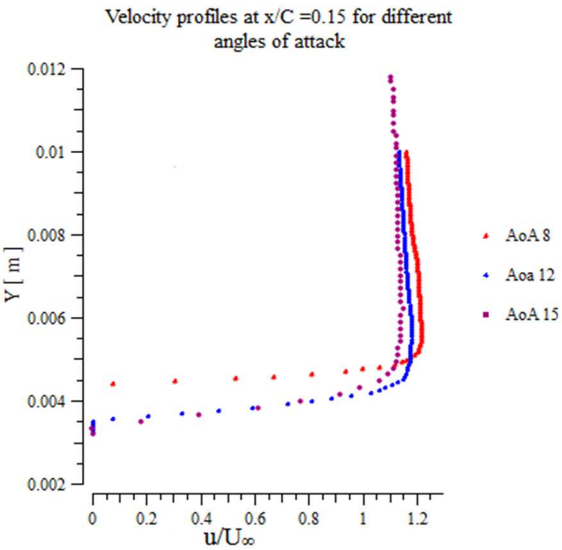

Fig. 9. Velocity profiles at x/C = 0.15 at different AoA

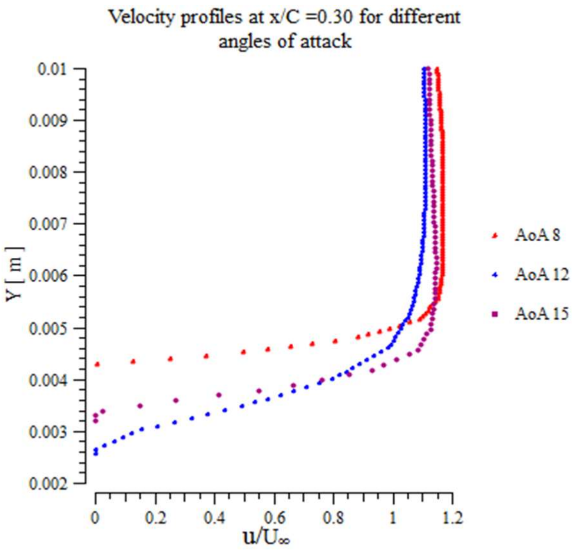

Fig. 10. Velocity profiles at x/C = 0.30 at different AoA

4.5 Effect of wingtip vortices at relatively high angles of attack

Wingtip vortices are strongly associated with an induced drag and induced drags comprise 30% of total drags for cruising flights. Therefore, it is important to study the characterization of wingtip vortices in order to reduce the induced drag. Any reduction in the strength of wingtip vortices will reduce the downwash on the wing at a given angle of attack, thereby resulting in a decrease in induced drags. The strength of wing-tip vortices is inversely proportional to the wing span and directly proportional to the speed of the aircraft, so during takeoff and landing the effect of induced drag is much more detrimental. The techniques for reducing the tip vortices include winglets, Ogee tips, and Raked wing tips.

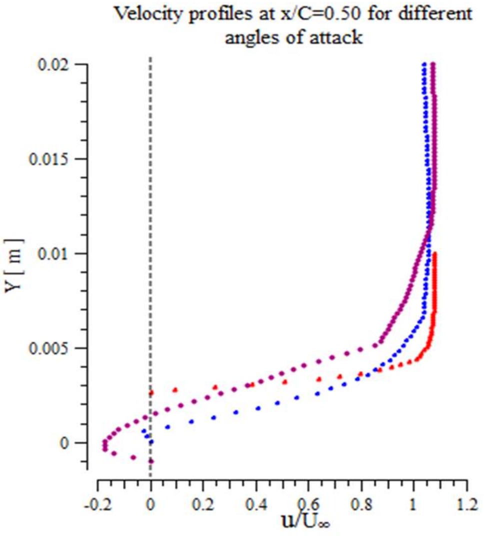

Fig. 11. Velocity profiles at x/C = 0.5 at different AoA

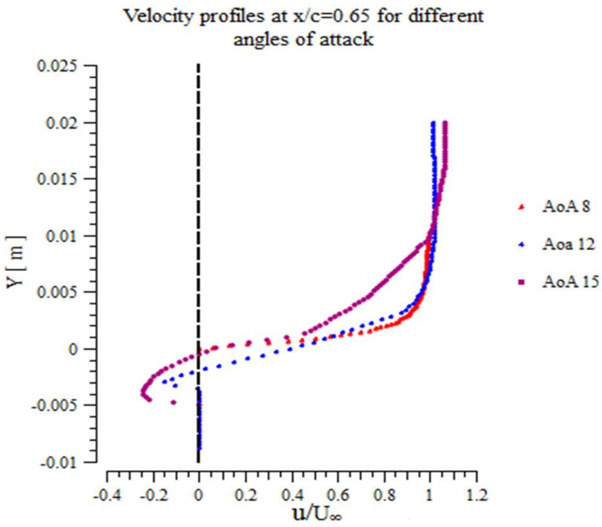

Fig. 12. Velocity profiles at x/C = 0.65 at different AoA

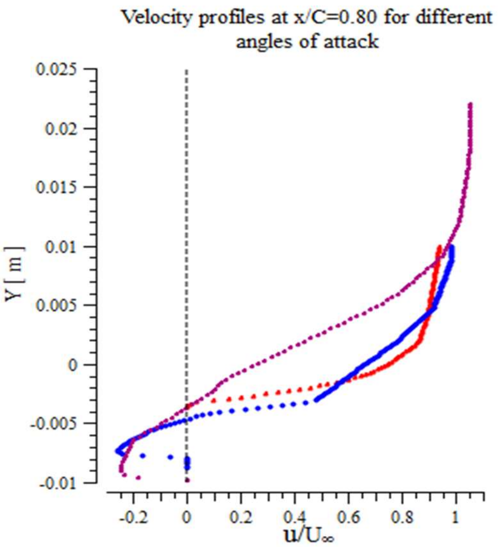

Fig. 13. Velocity profiles at x/C = 0.8 at different AoA

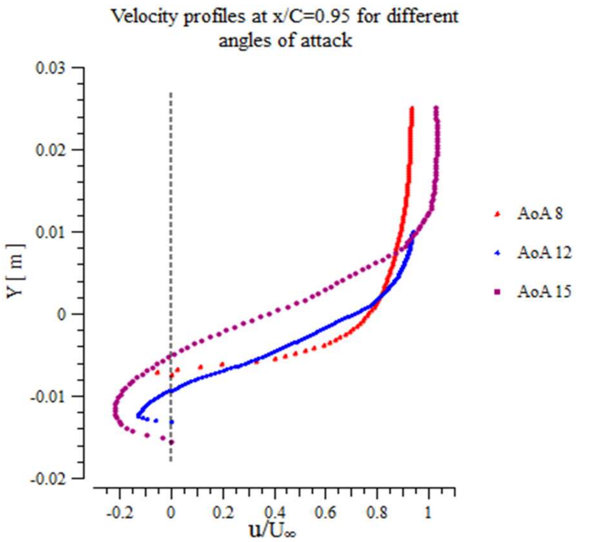

Fig. 14. Velocity profiles at x/C = 0.95 at different AoA

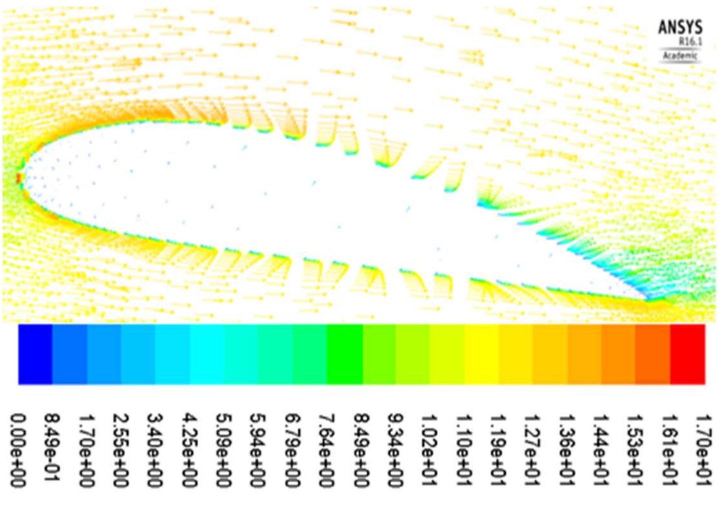

Fig. 15. Velocity vectors colored by velocity magnitude near wing tip region

Looking at the flow on a rectangular wing at an incidence in a region near the tip reveals that the streamlines on the upper surface try to bend towards the inboard of the wing whereas the flow on the lower surface tries to move towards the tip. This roll up of velocity vectors is observed to originate near the leading edge where the flow is accelerated from the lower surface to the upper surface and is wrapped around the tip. In details, with the development of this process near the tip, the flow coming from the lower surface encounters a strong adverse pressure gradient which eventually leads to separation by the cross flow velocity vectors in conjunction with the flow in the stream-wise direction and forms a vortex structure with a strong helical motion. The flow physics is highly turbulent and three–dimensional. It involves a high velocity gradient and this vortex structural flow forms the trailing vortex when it moves downstream of the trailing edge. Although rectangular wings generally stall around root region of the wing, still the effect of wing-tip region is an important part to be studied. Boundary layer interaction near the tip region has been studied and attempts have been made to explain the effect of wing-tip vortices at high AoA aerodynamics. It is very difficult to measure the size of wing-tip vortices. The size of wing-tip vortices over the wing surface is measured by the boundary layer interaction [Fig.15]. Although this is an approximate study, as this flow is highly unsteady and turbulent, we can easily understand the effect of wing-tip vortices for high AoA from this analysis.

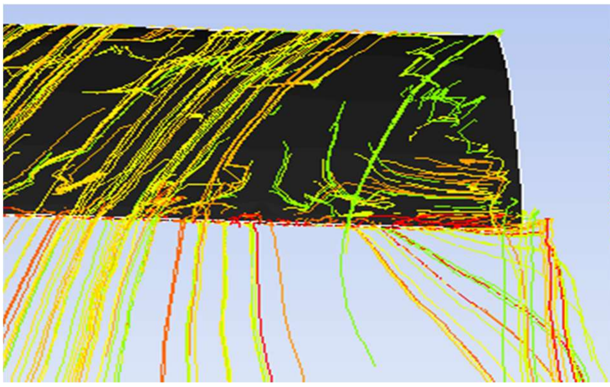

Fig. 16. Wing tip vortices at 4° AoA

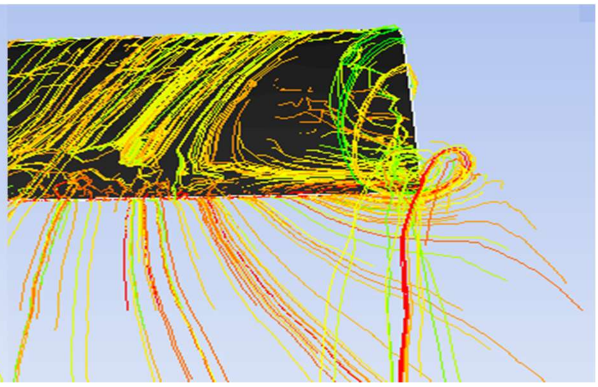

Fig. 17. Wing tip vortices at 8° AoA

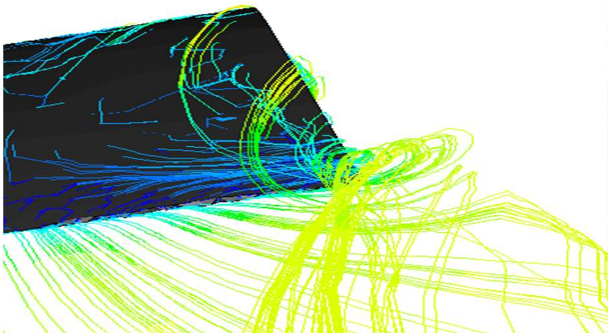

Fig. 18. Wing tip vortices at 12° AoA

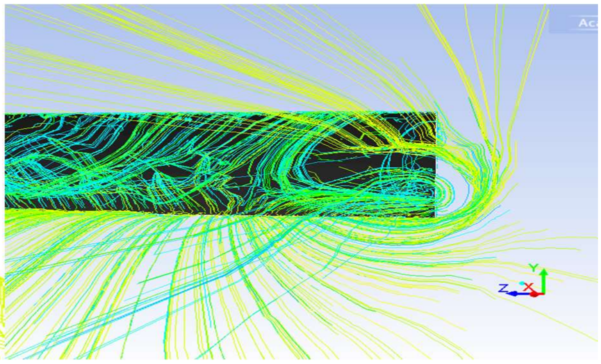

Fig. 19. Wing tip vortices at 15° AoA

Figs. 16 to 19 show the computed path line near the tip region in order to better understand the flow physics of wing-tip vortices. For the lower AoAs, the strength of coiling two velocity components is lower but as the AoA increases, the size of tip vortex increases. For lower angles of attack, the effect of the interaction of two boundary layers is beneficial since they will shed on the wing upper surface. For higher AoA, however, they will no longer shed on the surface of the wing and create a large wake region. Fig. 20 represents the variation in the diameter of wing-tip vortices at different angles of attack.

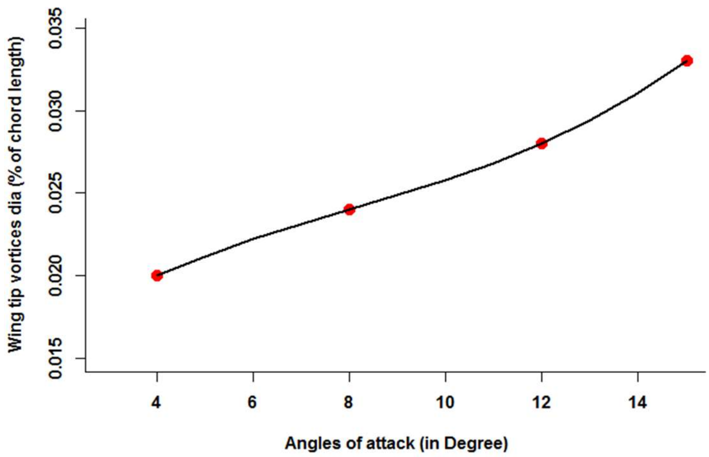

Fig. 20. Variation of tip vortices diameter with AoA

5. Conclusion

In this study, aerodynamic performance and flow separation behavior over a rectangular wing (NACA4415) was numerically investigated using experimental and ANSYS FLUENT analyses. For the higher Re (0.1 million), it was found that the recovery of lift coefficient of the wing is less pronounced compared to the lower Re (0.045 million). From the drag polar plot, it was observed that the maximum C_L/C_D is obtained at about 4°-6°, which can be considered significant for early capture of energy of small scale of HAWT applications (ANSYS FLUENT). For variable inflow conditions, it was found that thick airfoils give better performance at low Re [26] for their gentle stall behavior, which is well justified by the experimental result. In another case, at any given Re, the separation points were found to move from trailing edge to leading edge, which is expected since NACA4415 shows trailing edge stall behavior. It is very important to study the behavior of separation point accurately, based on which separate controllers are used for controlling flow separation at high AoAs. Another important study was conducted to measure the size of wing-tip vortices in order to reduce the induced drag and, to this end, we needed to have a fair idea on variation of the size of tip vortices with AoAs. Here, a different kind of method was introduced to measure it by measuring the size of boundary layer interaction zone near the wing-tip region. It was found that the size of wing-tip vortices is increased by an increase in AoA, which is quite obvious.

Nomenclature

Re	Reynolds number ($Re = \rho L^* U_{ref} / \mu$)
ξ	Boundary – layer co-ordinate
u_e	Edge velocity
H	Shape factor ($H = \delta^* / \theta$)
θ	Boundary Layer Momentum thickness
C_f	Skin friction coefficient, ($C_f = \tau / 0.5\, \rho U_{ref}^2$)
δ^*	Boundary – layer Displacement Thickness
$\rho\, u_e^2\, \theta$	Total Momentum Defect
α	Angles of attack (degrees)
x / C	Axial distance over airfoil axial chord (m)
μ	Molecular viscosity (Pa.sec)
μ_t or ε	Eddy viscosity (Pa.sec)
ω	Specific turbulence dissipation rate (m2 s-1)
k	Turbulent kinetic energy (J kg-1)
y	Distance from nearest wall (m)
y^+	Non-dimensional normal distance from wall-adjacent cell center
C_l	Coefficient of lift, ($C_l = L/0.5\rho U^2\ S^*$)
C_d	Coefficient of drag, ($C_d = D/0.5\rho U^2\ S^*$)
C_{lmax}	Maximum value of coefficient of lift
C_p	Coefficient of pressure, ($C_p = P/0.5\rho U^2\ S^*$)
L/D	Lift to drag ratio, ($L/D = C_l / C_d$)
L	Lift (N m-1)
D	Drag (N m-1)
AoA	Angles of attack
LSB	Laminar separation bubble
$NACA$	National Advisory Committee for Aeronautics

References

[1] Lissaman, P.B.S., Low-Reynolds-number-airfoils, *Annual Review Fluid Mechanics*, 15, 1983, 223-239.

[2] Carmichael, B.H., Low Reynolds Number Airfoil Survey, *NASA CR-165803*, 1, 1981, 19820006186.

[3] Sharma, M.S., Poddar, K., Experimental investigation of laminar separation bubble for a flow past an airfoil, *Proceedings of ASME Turbo Expo 2010: Power for Land*, Sea, and Air (GT2010), Glasgow, UK, 2010.

[4] Shah, H., Bhattarai, N., Lim, C.M., Mathew, S., Low Reynolds number airfoil for small horizontal axis wind turbine blades, Sustainable future energy 2012 and 10th SEE FORUM, Brunei Darussalam, 2012.

[5] Selig, M.S., Lecture notes on low Reynolds number airfoil design, *VKI lecture series 8*, 2003.

[6] Langtry, R.B., Menter, and F.R., Transition modeling for general CFD applications in aeronautics, 43rd AIAA Aerospace Sciences Meeting and Exhibit Reno, Nevada, 2005.

[7] Canonsburg, D.R., Fluent Theory Guide, *ANSYS Academic Research*, Canonsburg, 2011.

[8] Menter, P.R., Langtry, R., Voker, S., Transition modelling for general purpose CFD codes, *Flow, Turbulence and Combustion*, 77, 2006, 277–303.

[9] Menter, F., Zonal Two Equation K-ω Turbulence Models for Aerodynamic Flows, *23rd Fluid Dynamics, Plasma dynamics, and Lasers Conference*, Orlando, FL, U.S.A., 1999.

[10] Menter, F.R., Improved Two-Equation k-ω Turbulence Models for Aerodynamic Flows, *NASA Technical Memorandum*, 103975, October, 1992.

[11] Eggenspieler, G., Modelling Laminar Turbulent Transition Processes, ANSYS guide.

[12] PADT Lunch & Learn Series, ANSYS Meshing Advanced Techniques.

[13] Jones, B.M., Stalling, *J. R. Aeronaut. Soc.*, 38, 1934, 753–770.

[14] White, N.F., *Fluid Mechanics*, McGraw Hill series in Mechanical Engineering, 5th edition. McGraw Hill, New York, 2002.

[15] Hu, H., Yang, Z., An Experimental Study of the Laminar Flow Separation on a Low-Reynolds-Number Airfoil, *Journal of Fluids Engineering*, 130(5), 2008, 051101.

[16] Hatman, A., and Wang, T., A Prediction Model for Separated Flow Transition, *Journal of Turbo Machinery*, 121, 1999, 594–602.

[17] Solomon, W.J., Walker, G.J., Gostelow, J.P., Transition Length Prediction for Flows with Rapidly Changing Pressure Gradients," *Journal of Turbo Machinery*, 118, 1996, 744–751.

[18] Volino, R.J., Hultgren, L.S., Measurements in Separated and Transitional Boundary Layers Under Low-Pressure Turbine Airfoil Conditions, *Journal of Turbo Machinery*, 123, 2001, 189–197

[19] Lin, J.C.M., Pulley, L.L., Low-Reynolds-Number Separation on an Airfoil, *AIAA Journal*, 348, 1996, 1570–1577.

[20] Eastman, J., Sherman, A., Airfoil section characteristics as affected by variations of Reynolds number, NACA Report no. 586, 1937.

[21] McGranahan, B.D., Selig, M.S., Surface oil flow measurements on several airfoils at low Reynolds number, 21st AIAA Applied Conference, Orlando, Florida, 2003.
[22] Suzen, Y.B., Huang, P.G., Predictions of separated and transitional boundary layers under low-pressure turbine airfoil conditions using an intermittency transport equation, *Journal of Turbo Machinery*, 125, 2003, 455-464.
[23] Mueller, T.J., Batil, S.M., Experimental studies of separation on a two-dimensional airfoil at low Reynolds numbers, *AIAA Journal*, 20, 1982, 457–463.
[24] Cebeci, T., Mosinskis, G.J., Calculation of Separation Points in Incompressible Turbulent Flows, *Journal of Aircraft*, 9, 1972, 618-624.
[25] Stratford, S., The Prediction of Separation of the Turbulent Boundary Layer, *Journal of Fluid Mechanics*, 5, 1959, 1-16.
[26] Hansen, M.O.L., Aerodynamics of wind turbines, Routledge, 2013.
[27] Van den Berg, B., Role of Laminar Separation Bubbles in Airfoil Leading-Edge Stalls, *AIAA Journal*, 19(5), 1981, 553-556.
[28] Samal, S.K., Dash, P.K., Reduction of Wingtip Vortices by Using Active Means, *International Journal of Scientific & Engineering Research*, 4(4), 2013, 1280-1293.
[29] Wu, J.M. et al., Wing tip jets aerodynamics performance," 13th Congress of the International Council of the Aeronautical Sciences/AIAA Aircraft Systems and Technology Conference, ICAS proceedings, 2, 1982, 1115-1121.
[30] Wilcox, D.C., Reassessment of the Scale-Determining Equation for Advanced Turbulence Models, *AIAA Journal*, 26, 1988, 1299-1310.
[31] Coakley, T.J., Turbulence Modeling Methods for the Compressible Navier-Stokes Equations, *AIAA*, 83, 1982.
[32] W'ilcox, D.C., Rubesin, M.W., Progress in Turbulence Modeling for Complex Flow Fields Including the Effect of Compressibility, *NASA TP-1517*, 1980
[33] Johnson, D.A., King, L.S., A Mathematically Simple Turbulence Closure Model for Attached and Separated Turbulent Boundary Layers, *AIAA Journal*, 23, 1985, 1684-1692.
[34] An Introduction to Turbulence and Its Measurement, Pergamon, Oxford, 1975
[35] Cebeci, T., Bradshaw, P., Momentum Transfer in Boundary Layers, Hemisphere, New York, 1977.
[36] Shah, H., Mathew, S., Lim, C.M., Numerical simulation of flow over an airfoil for small wind turbines using the γ-Re_Θ model, International Journal of Energy and Environmental Engineering, 6(4), 2015, 419–429.
[37] J.D Anderson, *Fundamentals of Aerodynamics*, McGraw-Hill Education, 5th edition, February 12, 2010.
[38] Moffat, R.J., Using uncertainty analysis in the planning of an experiment, *Journal of Fluids Engineering*, 107(2), 1985, 173-178.
[39] Kline, S.J., McClintock, F.A., Describing Uncertainties in Single-Sample Experiments, *Mechanical Engineering*, 75(1), 1953, 3-8.